

POLITECNICO DI TORINO

Master Degree in Aerospace Engineering



Master's Degree Thesis

Aerodynamic performance of different airfoils for a future Mars Helicopter

Supervisors:

Prof. Akira Oyama (JAXA)
Prof. Gaetano Iuso (Politecnico di Torino)

Candidate

Lorenzo Bruni

July 2020

INDEX

ABSTRACT	3
1. INTRODUCTION.....	3
1.1. MOTIVATION FOR HELICOPTER FLIGHT ON MARS	4
1.2. MARS HELICOPTER MISSIONS.....	4
1.3. JAXA'S HELICOPTER	6
2. PURPOSE AND EXPERIMENTAL SET UP	7
2.1. MATHEMATICS	7
2.2. LIFT MEASURING DEVICE.....	8
2.3. ELECTRONICS.....	10
2.4. VACUUM CHAMBER.....	11
2.5. GRAPHICAL USER INTERFACE.....	12
2.6. BLADE PROFILES.....	13
2.6.1. <i>DF102</i>	13
2.6.2. <i>E178</i>	14
2.6.3. <i>E10</i>	15
2.6.4. <i>Triangular Profile</i>	16
2.6.5. <i>Nominal</i>	19
2.7. DIFFICULTIES	23
3. POST PROCESSING.....	24
3.1. NEW ROTOR DESIGN	33
4. CONCLUSIONS	34
4.1. POSSIBLE FUTURE WORK.....	34
5. APPENDIX.....	35
5.1. HOVERING HELICOPTER THRUST	35
5.2. EXPERIMENTAL AIRFOIL FOR ULTRA LOW REYNOLDS NUMBER.....	37
5.3. WEIGHT REDUCTION	39
BIBLIOGRAPHY	40

Abstract

Aerodynamic evaluation of multiple blade profiles for a future Mars helicopter is presented using vacuum chamber experiments. A small-scale Mars helicopter prototype, that was chosen to explore deep craters present on the red planet surface, was fastened to a specifically designed test structure and the generated thrust was then measured for different airfoils, rotor speeds and angles of attack. Afterwards, thrust coefficients were extrapolated from these measurements and compared with one another leading to interesting results such as performance improvement with decreasing thickness and increasing camber, good performance of triangular airfoils and E178 airfoil improving performance with decreasing Reynolds.

1. Introduction

In recent years, space exploration agencies have increased their interest towards Mars, with the intention of studying its evolution, searching for life and fostering human missions. As of 2020 only wheeled rovers have been used to scout the red planet's surface. These vehicles, although being very slow, have been very useful for unprecedented exploration of the planet. However, engineers have started to think about using flying objects, such as small helicopters or airplanes, to scout the surface or achieve operations that normal rovers would not be able to perform. There are many mission concepts regarding the use of a compact self-flying helicopter; however, all of them have in common the need for unique design methods and flight configurations. This is due to Mars' environment being unfavorable to flight, as characterized by an atmospheric pressure near the surface of about 1% of that of Earth and an atmospheric density that is as low as $0.0121 \frac{Kg}{m^3}$. Further compounding these issues is Mars' cold carbon dioxide atmosphere which, given a lower Mach number compared to Earth's, induces compressibility effects to appear sooner on the rotor blades. Compressibility effects introduce a high increase in wave drag and the possibility to reach sonic speeds on the blade, generating normal shocks that further break up the airflow and could possibly damage the blade itself. Fortunately, not everything is against the success of Mars flight as gravity is nearly 3 times lower on Mars, where gravitational acceleration is $3.71 \frac{m}{s^2}$ compared to Earth's $9.81 \frac{m}{s^2}$.

1.1. Motivation for helicopter flight on Mars

There are a few reasons why deploying a helicopter on Mars would be beneficial for future missions. As a start, an aircraft would be able to move much faster, covering more ground, while flying several meters above the ground achieving better views of what it has around with respect to a rover.

In addition, a peculiar feature of the Mars surface is the presence of lava tubes. A lava tube is a natural conduit formed by flowing lava, which moves beneath the hardened surface of its own flow. Tubes can be extinct, meaning the lava flow has ceased, and the rock has cooled down leaving a cave behind. Some sections of these tubes, the ones closer to the surface, can collapse creating a skylight.

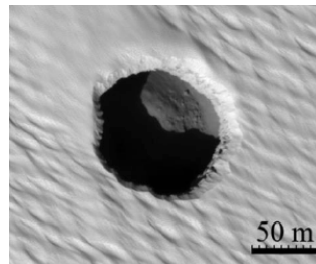


Figure 1 Pit crater on Mars surface.[28]

These skylights are attracting many scientists because it is considered that the observation of their inner wall could reveal the history of Mars' volcanic activity. In addition, the possibility of finding traces of life is discussed because of the lack of ultraviolet rays and other radiations from the Sun. For the same reason, engineers are considering the possibility of using lava tubes as bases for future manned missions. Due to their nearly vertical walls, however, ordinary rovers cannot be used to explore these craters. In their place these small sized, lightweight helicopters are intended to be used, mainly for their ability to execute Vertical Take-Off and Landing (VTOL).

1.2. Mars helicopter Missions

Although their mission concepts and objectives are quite different, two main companies are currently working on a Mars helicopter: JAXA and NASA.

NASA is planning to use its already built and tested Mars helicopter during the Mars 2020 mission, which is launching in July 2020 [29]. The 1.8 Kg helicopter, in figure 2, consists on counter-rotating coaxial rotors of about 1.1 m in diameter (tapered, twisted and 10 cm in chord length) spinning between 1900 and 2800 rpm [20, 30]. A high-resolution downward-looking camera for navigation, landing, and science surveying of the terrain makes up its payload, this is added to a communication system that relays data to the rover. The main purpose of this helicopter is to assist the main rover "*Perseverance*". After two and half months from the landing, the aircraft will fly up to five times during the 30-day test period. Each flight will last up to 3 minutes, at altitudes ranging from 3 m to 10 m above ground, while the distance covered is thought to reach as far as 300 m per flight. It will make use of autonomous control and will communicate with the *Perseverance* rover directly after each landing while recharging through its own solar panel. The helicopter will be able to provide overhead images with approximately ten times the resolution of orbital images, displaying features that are most likely occluded from the rover cameras. This scouting method could

enable improved road mapping thus allowing future rovers to safely drive up to three times as far per sol. The mission is thus only a support operation for the rover, which is the main scope of the expedition.

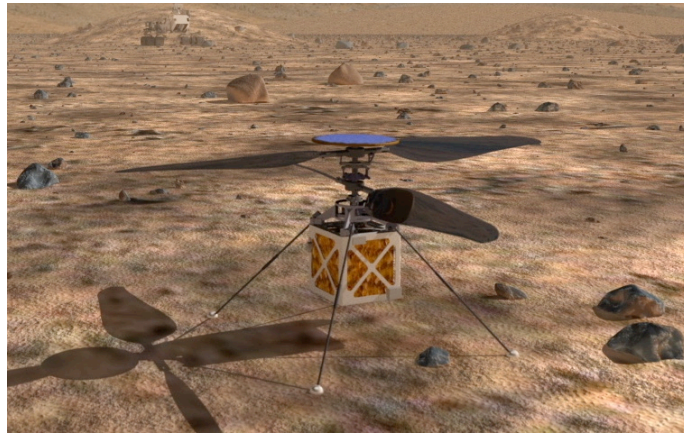


Figure 2 NASA's Mars helicopter concept. [17]

On the other hand, JAXA's mission foresees a helicopter piggybacking on a rover to the crest of a lava pit, where it then proceeds to hover inside of the tube mapping the conduit, taking pictures and sampling the walls. It then returns on top of the rover where it will be recharged and either a new path is planned for the same duct or the aircraft is relocated for the next assignment. Compared to NASA's mission, JAXA's is more focused on the helicopter and the rover is only a support for the main task. The helicopter is thus required to be able to fly for as much time as possible. This research is focused on improving the JAXA's helicopter aerodynamic properties since the more efficient its aerodynamics the less power it will require to generate the same amount of thrust, thus increasing flight time.

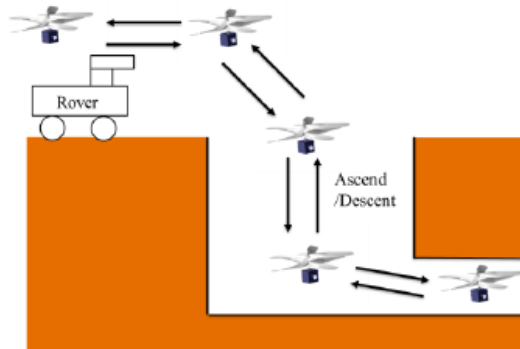


Figure 3 JAXA's mission concept. [14]

1.3. JAXA's Helicopter

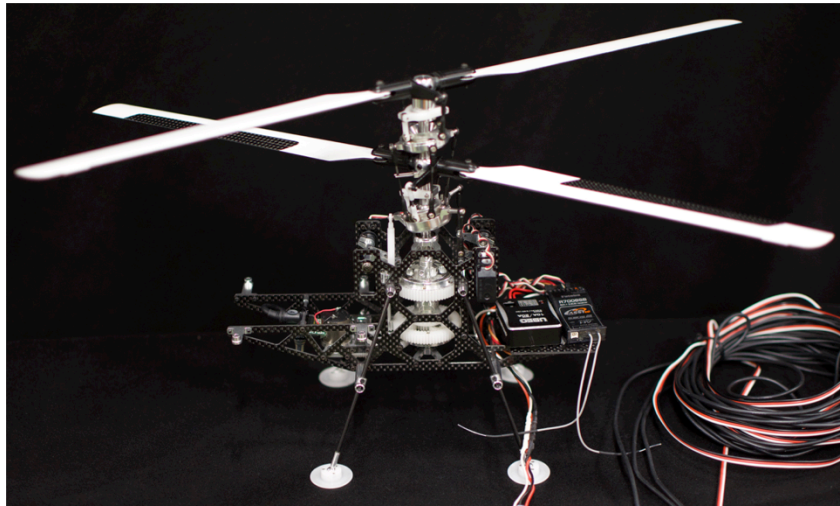


Figure 4 JAXA's Mars helicopter.

As shown in figure 4, this 465 grams helicopter has two coaxial counter rotating propellers. According to reference [21], this was chosen in order to maximize thrust production operating at the same power, and to eliminate the effect of having a non zero total torque on the body. The propellers are mounted on a carbon-fiber chassis and driven by a high efficiency electric motor through appropriately dimensioned gears such that at 100% motor usage, the propeller reaches 2500 rpm. Two different remotes can control the helicopter. One remote controls solely its angular velocity. The other controls its pitch, roll, yaw and collector by directly moving the helicopter' swash plate or, in case of yaw, overriding the first controller triggering the propellers to rotate in the same direction affecting angular momentum and creating a strong enough torque that induces the helicopter to turn on itself.



5 Mars controllers. RPM manager (left) all movement remote (right)

2. Purpose and Experimental Set Up

The goal of these experiments was to understand how rotational speed, blade chord, and blade profile affect thrust production of a small-scale helicopter prototype in a simulated Martian environment characterized by an ultra low Reynolds number flow. This was carried out by positioning the JAXA's helicopter in a device that constraints every degree of freedom except for vertical motion. An S-shaped strain sensor was then linked to the helicopter in order to block the vertical motion while measuring how much thrust was being generated. This whole device was then put inside of a vacuum chamber and brought from 1kPa to 5 kPa with a 1-kPa step. Once at the desired pressure the rotor was sped up from 2000 to 2500 rpm with a 250-rpm step. At each step the blade pitch angle was shifted from 0 to 18 degrees with 3 degrees step. This pitch angle was measured from the fundamental horizontal using a digital level. Because of swash plate design and positioning on the main shaft, 18 degrees was the maximum mechanically reachable pitch angle.

2.1. Mathematics

Given the equation for lift produced by a double rotating disk (calculated in the appendix):

$$T = 2\rho C_T A \Omega^2 R^2 \quad (1)$$

Where,

C_T = Thrust coefficient

ρ = Air density

A = Disk area, proportional = πR^2

Ω = Rotor angular speed

R = Rotor radius

Thrust coefficient can thus be extrapolated as:

$$C_T = \frac{T}{2\rho A \Omega^2 R^2} \quad (2)$$

From equation (1) the formula for radius can also be composed. This equation was used at the end of the research to compute the ideal radius length:

$$R = \left(\frac{T}{2\rho \pi C_T \Omega^2} \right)^{\frac{1}{4}} \quad (3)$$

After all of the experiments, the results will be shown at the same Reynolds number conditions so that the flow characteristics are equal for each. Therefore this parameter's equation is shown below:

$$Re = \frac{\rho V L}{\mu} \quad (4)$$

Where,

ρ = Air density [$\frac{Kg}{m^3}$]

V = Rotor speed at $\frac{3}{4}$ of the blade length, where the major part of the thrust is generated [$\frac{m}{s}$]

L = Chord length [m]

μ = Air dynamic viscosity [$Pa * s$]

The gas density was easily calculated by using the ideal gas law:

$$\rho = \frac{P\mathcal{M}}{RT} \quad (5)$$

Where,

P = Air pressure [Pa]

\mathcal{M} = Molar mass, 29 $[\frac{Kg}{Mol}]$ for air

T = Air temperature [K]

R = Gas universal constant, 8314 $[\frac{J}{K*Mol}]$

On the other hand, the Sutherland law, shown below, was implemented to calculate dynamic viscosity:

$$\mu = \mu_0 * \left(\frac{T_0 + C}{T + C}\right) * \left(\frac{T}{T_0}\right)^{\frac{3}{2}} \quad (6)$$

Where,

μ_0 = Reference viscosity, for air $1.716*10^5 [Pa * s]$

T_0 = Reference Temperature, 273.15 [K]

T = Temperature at which viscosity is calculated

C = Sutherland's constant, 110.4 [K] for air

2.2. Lift Measuring Device

The Lift Measuring Device (LMD) was designed to stop any movement except for vertical motion. This way the helicopter was able to fly safely without any stabilization control, which gave the possibility to take a few shots of the flying helicopter to prove the feasibility of the project. After taking these shots the helicopter was anchored to the base of the structure through an S-shaped strain sensor. At rest, the sensor completely withstood the helicopter weight. When the helicopter started producing thrust the weight on the sensor reduced letting the sensor expand. This expansion is translated from electrical signals to grams thus measuring thrust produced. The whole device, as depicted in figure 6, was first designed on *Autodesk's Inventor Professional*, part by part and then assembled. Due to their criticality, some parts were first 3D printed in PLA using a *MakerBot Replicator 2* printer in order to check the correctness of their design. Once every part was checked and confirmed to be correct, the device was built resulting in what is shown in figure 10. From equation (1) it could be easily seen that thrust was directly proportional to the squared power of Ω and to the fourth power of R. For preliminary calculation C_T was chosen as 0.0063, value taken from the previous work done by *Aoki* in reference [22]. Thus in an ideal environment a large radius along with slow angular velocity is preferred. However, there were a few issues. To start, as radius increased the helicopter size increased making it difficult to perform experiments inside of the vacuum chamber. In addition, the motor used in the helicopter had better efficiency at high speeds (of around 10000 rpm or above [11]). It was also decided that the Mach number at the tip should have been lower than 0.85 to avoid drag divergence due to shockwaves.

That Mach number value was chosen for the following reasons:

- Local Mach number should have always been lower than 1 to remain subsonic.
- Once deployed the helicopter will move forward or backward creating relative velocities, which will increase and decrease the blades' Mach number.
- Due to its low temperature carbon dioxide based atmosphere ($\gamma=1.28$, $\mathcal{M}= 44.01 \frac{g}{mol}$), Mars' speed of sound is lower than the one on Earth which means that a lower flight speed is required to reach the critical Mach number.

A maximum radius of 0.5 m with an angular velocity of maximum 5000 rpm (Mach = 0.77) was considered, causing the ideal generated thrust to be around 8.21 N. For longer radii the usable Ω was too low, and more importantly, the helicopter would not have fit inside of the vacuum chamber. However, the weight of the 0.5 m blades was too large to be handled by the small helicopter: the centrifugal force would have broken the aircraft apart. Thus it was decided to use small rotors with different airfoils, explained in details in chapter 2.6. An additional factor was taken into account: Mars has a lower gravity pull than Earth. The actual weight of the helicopter drops substantially from 4.52 N to 1.71 N. In order to study the feasibility of the flight, the helicopter should have been able to lift only its Martian weight. Thus, the need was raised to alleviate the helicopter from all of the structure weight as well as part of its own. This was carried out securing a total of 1.84 Kg (mass of the structure connected to the helicopter added to the weight that the helicopter would lose on Mars. Equation found in the Appendix) evenly divided between the two arms supporting the helicopter. The direction of the force induced by these weights was directed upward with respect to the arms using pulleys at the top of the structure in such a way that the masses would not hit the ground before the helicopter reached its imposed height limit.

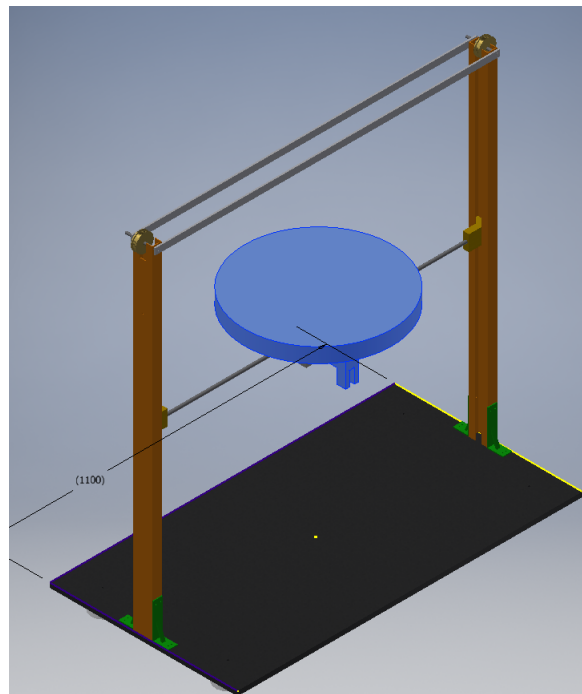


Figure 6 Lift Measuring Device project as seen from Inventor 3D.

2.3. Electronics

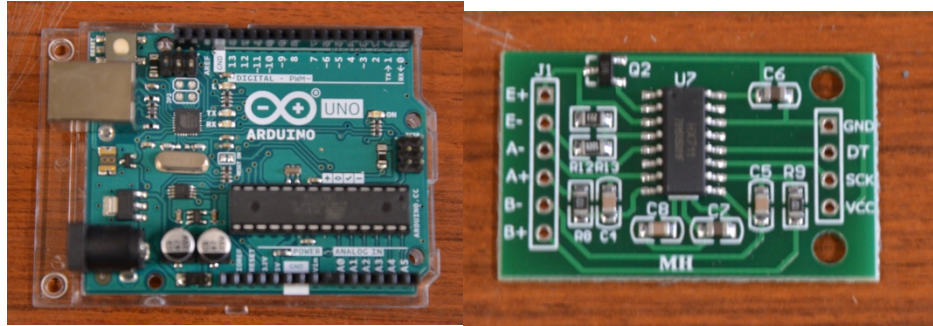


Figure 7 Arduino UNO board (left) and HX711 amplifier (right)

The whole case study's objective is based on lift measuring. This brought up the need to choose the right sensors, interfaces and microcontrollers. Arduino UNO was chosen as a microcontroller due to the low strain of the task and the board's low price and high quality performance. As explained before, the maximum lift expected was at first 8N. Since the helicopter will not always be able to lift itself up, a sensor able to measure both its own compression and tension was chosen. A sensor of this kind translates, through a Wheatstone bridge, the change in resistance, due to its own deformation after compression or tension, in electrical signals. The sensor selected was a 10N Unipulse USM full Wheatstone bridge sensor with a Rated Output (R.O.) of 0.4159 mV/V. Although the Arduino sensitivity is quite high, due to such low R.O., this sensor couldn't be directly linked with the microcontroller. Thus the HX711 board was used to amplify the readings of the USM sensor. This 10N sensor was only used to measure thrust at standard pressure. Inside of the vacuum test chamber, because of the forced choice of radius and speeds, a 2N USM sensor, shown in figure 8, was operated.

In order to minimize electrical noise, the sensor circuit was completely embedded into the vacuum chamber. Since Arduino permits connection through USB-A to USB-B ports a single cable was cut and extended in such a way that the thrust readings were done a few centimeters from the sensor and stored into the Arduino, which then relayed it to the PC through a 10 m cable. This way the analog voltage shift, which is easily corruptible by noise, was converted at once into grams and promptly sent through a digital signal to the outside computer. This, in addition to the fringe layout explained in the following section, ensured electrical noise to a minimum. Each experiment was carried out at least twice, and the 2N sensor's higher precision was used to confirm the values measured by the 10N sensor. As an example, if the 10N sensor detected a thrust of 10 g, the 2N sensor would perceive approximately the same value with a range of ± 0.8 g.

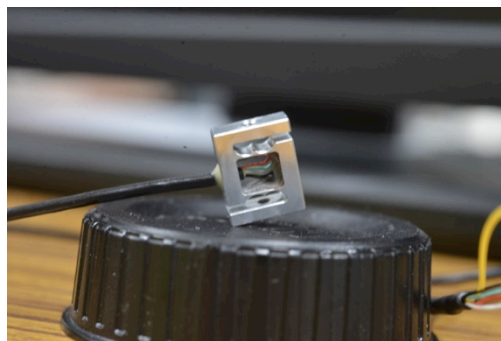


Figure 8 USM Unipulse 2N compression/tension sensor

2.4. Vacuum chamber

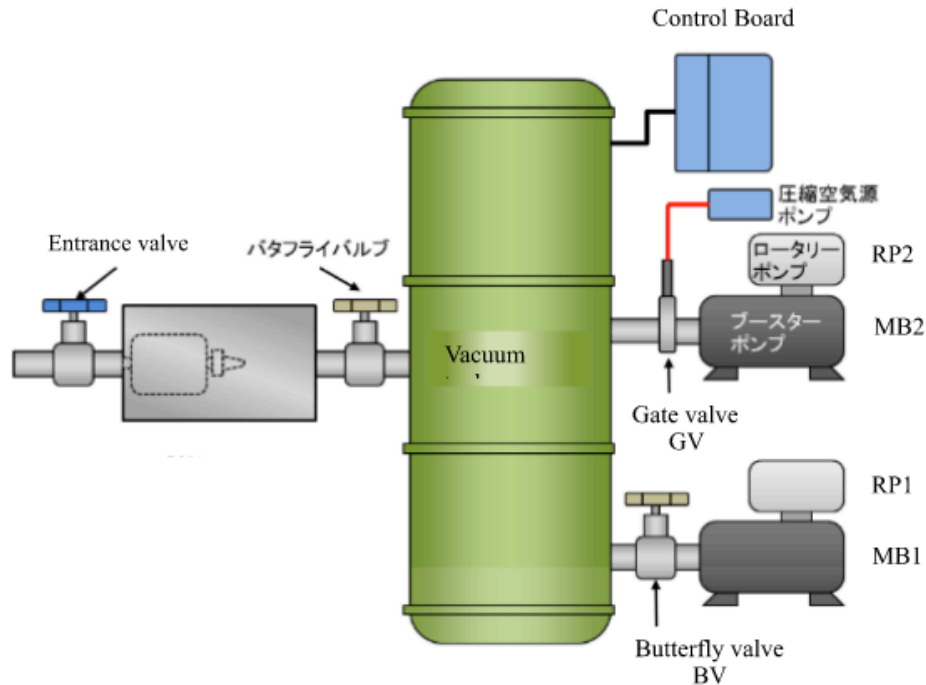


Figure 9 Vacuum chamber setup schematics.

The chamber used was a cylindrical steel structure 1.3 m wide and 7 m long powered by two rotary pumps. Alongside these two machines, two additional boost pumps were also present in order to lower the pressure below 2 kPa. The set up used two independent fringes of 16 and 10 cables in order to interface the helicopter with the outside computer and controllers. This interface tried to separate power lines from data lines in order to lower as much as possible electrical noise created by flowing high current. The 12 and 24 Volt cables, the motor drivers cables and the servo cables were all in one fringe, while the Radio frequency cable, the rpm control cables, and the Arduino USB cables were in the other. As explained before, the sensor circuit was completely inside the chamber minimizing cable length and thus noise.

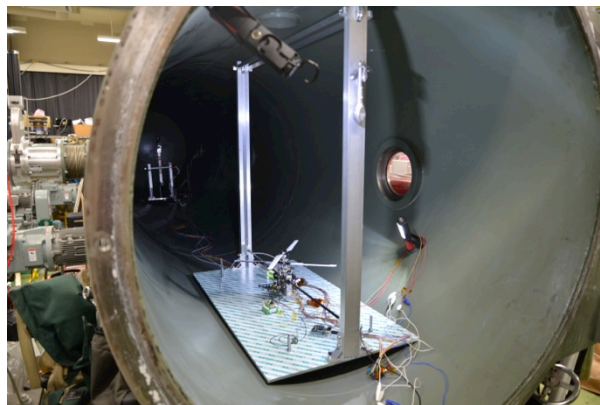


Figure 10 LMD fully constructed and inside of the vacuum chamber

2.5. Graphical User Interface

This experiment's GUI was fairly simple as the only checked parameters were pressure and thrust. "LabView" software was used to monitor pressure instant values in order to check if it remained constant over time, as one can see from figure 11. This output was also used to set the pressure at the desired value for each step of the experiment.

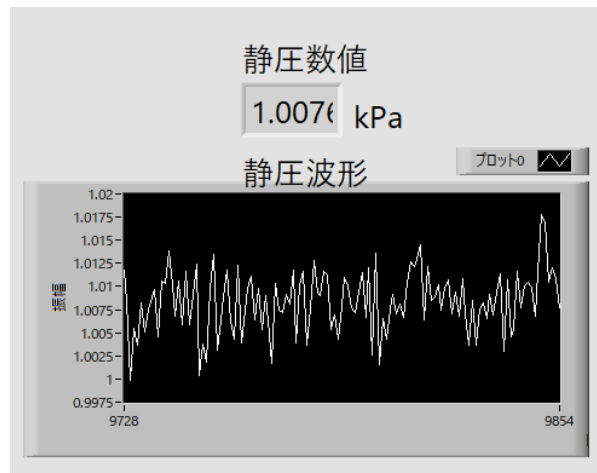


Figure 11 LabView window monitoring instant and waveform value for pressure.

As far as the force sensor is concerned, the Arduino IDE was used. Arduino permits machine serial communication whose output is shown in figure 12A, where an unloaded sensor's output is being displayed. The slight but constant decrease on measured thrust is due to an infinitesimal expansion of the sensor due to a temperature increase, which is caused by the electric current running through the Wheatstone resistors. It is worth noting that this small change in thrust is barely sensed when measuring an actual load as can be seen in figure 12B.

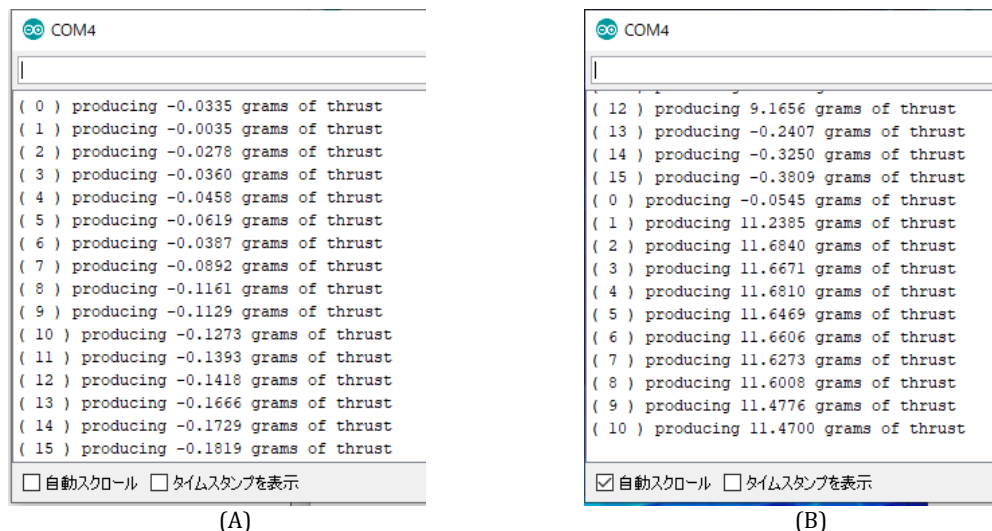


Figure 12 Arduino IDE visual output for zero load (A) and applied thrust (B).

2.6. Blade Profiles

Because of the limited usable radius it was decided to use a 3D printer to also build various blade profiles in order to understand their performance in an ultra low Reynolds number environment. DF102, E178 and E10 profiles were chosen, after a broad search of most low Reynolds number airfoils (designed for Re of about 70000) currently being used, due to their better performance [23, 27]. On the other hand, the triangular airfoil, specifically designed for Reynolds number 3000, was chosen to continue some promising previous and ongoing researches [6, 9, 24, 25, 26]. The *MakerBot Replicator 2*, showcased in figure 18, was again used. Although initially the blades should have been 0.23 m long to match the nominal blade length, due to some 3D printing limitations they had to be shortened to 0.17 m. Normal 1.75 mm PLA was used. Before being printed all the airfoils were carefully designed with *Autodesk Inventor 3D*. This software supports importing point coordinates that were downloaded from “*Airfoil tools*” website [23]. After being printed, each batch of blades was meticulously sandpapered to eliminate as much surface imperfection as possible. Each blade is now described and their experimental values, already translated into C_T , documented below.

2.6.1. DF102

The DF102 is a low Reynolds number airfoil with an 11% maximum thickness positioned at 29.1% chord and a maximum camber of 2.4% at 43.5% chord.

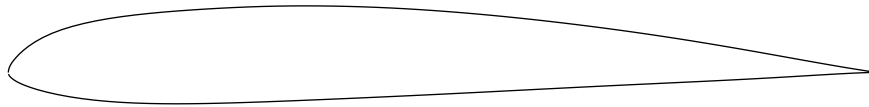


Figure 13 DF102 profile.

Values of C_T for a chamber pressure of 4 kPa and two speeds are reported below.

RPM	Pitch Angle [°]	C_T
2250	0	0.00000
	3	0.00039
	6	0.00078
	9	0.00234
	12	0.00546
	15	0.00780
	18	0.01170
2500	0	0.00000
	3	0.00126
	6	0.00253
	9	0.00316
	12	0.00568
	15	0.00821
	18	0.01011

Table 1 DF102 C_T values at 4kPa, 2250 and 2500 rpm, and all AOA.

Values of C_T for a chamber pressure of 5 kPa and two speeds are reported below.

RPM	Pitch Angle [°]	C_T
2250	0	0.00000
	3	0.00062
	6	0.00125
	9	0.00250
	12	0.00561
	15	0.00811
	18	0.01123
2500	0	0.00000
	3	0.00051
	6	0.00101
	9	0.00253
	12	0.00505
	15	0.00808
	18	0.01061

Table 2 DF102 C_T values at 5kPa, 2250 and 2500 rpm, and all AOA.

2.6.2. E178

The E178 is a low Reynolds number airfoil with an 8% maximum thickness positioned at 29.8% chord and a maximum camber of 2.8% at 38.8% chord



Figure 14 E178 profile.

Values of C_T for a chamber pressure of 4 kPa and two speeds are reported below.

RPM	Pitch Angle [°]	C_T
2250	0	0.00000
	3	0.00156
	6	0.00234
	9	0.00390
	12	0.00702
	15	0.01092
	18	0.01326
2500	0	0.00000
	3	0.00126
	6	0.00189
	9	0.00379
	12	0.00695
	15	0.00947
	18	0.01200

Table 3 E178 C_T values at 4kPa, 2250 and 2500 rpm, and all AOA.

Values of C_T for a chamber pressure of 5 kPa and two speeds are reported below.

RPM	Pitch Angle [°]	C_T
2250	0	0.00000
	3	0.00187
	6	0.00250
	9	0.00374
	12	0.00624
	15	0.00936
	18	0.01248
2500	0	0.00000
	3	0.00101
	6	0.00202
	9	0.00303
	12	0.00606
	15	0.00910
	18	0.01162

Table 4 E178 C_T values at 5kPa, 2250 and 2500 rpm, and all AOA.

2.6.3. E10

The E10 is a low Reynolds number airfoil with a maximum 10% thickness positioned at 31.9% chord and a maximum camber of 0.3% at 31.9% chord.

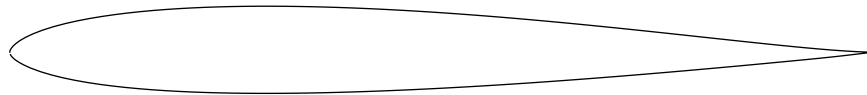


Figure 15 E10 profile.

Values of C_T for a chamber pressure of 4 kPa and two speeds are reported below.

RPM	Pitch Angle [°]	C_T
2250	0	0.00000
	3	0.00039
	6	0.00078
	9	0.00156
	12	0.00390
	15	0.00624
	18	0.00936
2500	0	0.00000
	3	0.00032
	6	0.00063
	9	0.00189
	12	0.00379
	15	0.00632
	18	0.00821

Table 5 E10 C_T values at 4kPa, 2250 and 2500 rpm, and all AOA.

Values of C_T for a chamber pressure of 5 kPa and two speeds are reported below.

RPM	Pitch Angle [°]	C_T
2250	0	0.00000
	3	0.00062
	6	0.00125
	9	0.00187
	12	0.00343
	15	0.00686
	18	0.00936
2500	0	0.00000
	3	0.00051
	6	0.00126
	9	0.00227
	12	0.00404
	15	0.00657
	18	0.00859

Table 6 E10 C_T values at 5kPa, 2250 and 2500 rpm, and all AOA.

2.6.4. Triangular Profile

The triangular airfoil chosen has a 10% maximum thickness positioned at 25% of the chord.



Figure 16 Triangular profile.

Values of C_T for a chamber pressure of 1 kPa and three speeds are reported below.

RPM	Pitch Angle [°]	C_T
2000	0	0.00000
	3	0.00000
	6	0.00039
	9	0.00079
	12	0.00158
	15	0.00434
	18	0.00513
2250	0	0.00031
	3	0.00125
	6	0.00156
	9	0.00250
	12	0.00499
	15	0.00686
	18	0.00936

2500	0	0.00051
	3	0.00177
	6	0.00253
	9	0.00531
	12	0.00632
	15	0.00808
	18	0.00935

Table 7 Triangular airfoil C_T values at 1kPa, all speeds, and all AOA.

Values of C_T for a chamber pressure of 2 kPa and three speeds are reported below.

RPM	Pitch Angle [°]	CT
2000	0	0.00000
	3	0.00000
	6	0.00118
	9	0.00158
	12	0.00414
	15	0.00671
	18	0.01066
2250	0	0.00047
	3	0.00140
	6	0.00296
	9	0.00390
	12	0.00795
	15	0.01029
	18	0.01310
2500	0	0.00076
	3	0.00189
	6	0.00265
	9	0.00341
	12	0.00619
	15	0.00935
	18	0.01200

Table 8 Triangular airfoil C_T values at 2kPa, all speeds, and all AOA.

Values of C_T for a chamber pressure of 3 kPa and three speeds are reported below.

RPM	Pitch Angle [°]	CT
2000	0	0.00013
	3	0.00053
	6	0.00184
	9	0.00329
	12	0.00658
	15	0.00908
	18	0.01118

2250	0	0.00031
	3	0.00083
	6	0.00260
	9	0.00478
	12	0.00780
	15	0.01164
	18	0.01393
2500	0	0.00034
	3	0.00101
	6	0.00244
	9	0.00404
	12	0.00707
	15	0.00994
	18	0.01263

Table 9 Triangular airfoil C_T values at 3kPa, all speeds, and all AOA.

Values of C_T for a chamber pressure of 4 kPa and three speeds are reported below.

RPM	Pitch Angle [°]	C_T
2000	0	0.00030
	3	0.00089
	6	0.00188
	9	0.00345
	12	0.00641
	15	0.00947
	18	0.01174
2250	0	0.00078
	3	0.00203
	6	0.00390
	9	0.00491
	12	0.00850
	15	0.01209
	18	0.01497
2500	0	0.00063
	3	0.00133
	6	0.00265
	9	0.00411
	12	0.00701
	15	0.01017
	18	0.01288

Table 10 Triangular airfoil C_T values at 4kPa, all speeds, and all AOA.

Values of C_T for a chamber pressure of 5 kPa and three speeds are reported below.

RPM	Pitch Angle [°]	C_T
2000	0	0.00039
	3	0.00095
	6	0.00229
	9	0.00363
	12	0.00679
	15	0.00995
	18	0.01216
2250	0	0.00056
	3	0.00125
	6	0.00318
	9	0.00474
	12	0.00867
	15	0.01223
	18	0.01566
2500	0	0.00051
	3	0.00116
	6	0.00258
	9	0.00404
	12	0.00728
	15	0.01046
	18	0.01319

Table 11 Triangular airfoil C_T values at 5kPa, all speeds, and all AOA.

2.6.5. Nominal

Nominal blade is a NACA 0015 airfoil. Maximum thickness is 15% positioned at 30% of the chord.

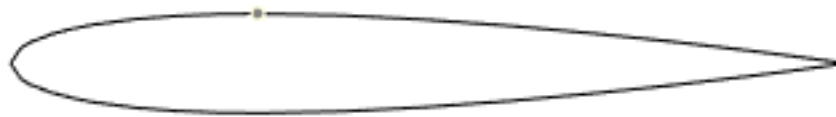


Figure 17 NACA 0015 profile.

Values of C_T for a chamber pressure of 1 kPa and three speeds are reported below.

RPM	Pitch Angle [°]	C_T
2000	0	0.00000
	3	0.00022
	6	0.00044
	9	0.00154
	12	0.00198
	15	0.00264
	18	0.00352

2250	0	0.00000
	3	0.00043
	6	0.00070
	9	0.00174
	12	0.00243
	15	0.00356
	18	0.00426
2500	0	0.00000
	3	0.00042
	6	0.00091
	9	0.00127
	12	0.00246
	15	0.00317
	18	0.00359

Table 12 NACA 0015 C_T values at 1kPa, all speeds, and all AOA.

Values of C_T for a chamber pressure of 2 kPa and three speeds are reported below.

RPM	Pitch Angle [°]	CT
2000	0	0.00000
	3	0.00016
	6	0.00049
	9	0.00121
	12	0.00231
	15	0.00297
	18	0.00357
2250	0	0.00000
	3	0.00026
	6	0.00100
	9	0.00156
	12	0.00287
	15	0.00400
	18	0.00487
2500	0	0.00000
	3	0.00021
	6	0.00053
	9	0.00144
	12	0.00225
	15	0.00317
	18	0.00391

Table 13 NACA 0015 C_T values at 2kPa, all speeds, and all AOA.

Values of C_T for a chamber pressure of 3 kPa and three speeds are reported below.

RPM	Pitch Angle [°]	C_T
2000	0	0.00000
	3	0.00015
	6	0.00070
	9	0.00150
	12	0.00231
	15	0.00337
	18	0.00414
2250	0	0.00000
	3	0.00017
	6	0.00072
	9	0.00180
	12	0.00272
	15	0.00353
	18	0.00492
2500	0	0.00000
	3	0.00016
	6	0.00070
	9	0.00129
	12	0.00232
	15	0.00331
	18	0.00411

Table 14 NACA 0015 C_T values at 3kPa, all speeds, and all AOA.

Values of C_T for a chamber pressure of 4 kPa and three speeds are reported below.

RPM	Pitch Angle [°]	C_T
2000	0	0.00000
	3	0.00016
	6	0.00069
	9	0.00121
	12	0.00231
	15	0.00346
	18	0.00421
2250	0	0.00000
	3	0.00035
	6	0.00089
	9	0.00156
	12	0.00280
	15	0.00404
	18	0.00517

2500	0	0.00000
	3	0.00019
	6	0.00069
	9	0.00128
	12	0.00239
	15	0.00357
	18	0.00442

Table 15 NACA 0015 C_T values at 4kPa, all speeds, and all AOA.

Values of C_T for a chamber pressure of 5 kPa and three speeds are reported below.

RPM	Pitch Angle [°]	C_T
2000	0	0.00000
	3	0.00026
	6	0.00077
	9	0.00128
	12	0.00231
	15	0.00334
	18	0.00433
2250	0	0.00000
	3	0.00021
	6	0.00090
	9	0.00148
	12	0.00280
	15	0.00417
	18	0.00528
2500	0	0.00000
	3	0.00023
	6	0.00077
	9	0.00139
	12	0.00246
	15	0.00369
	18	0.00469

Table 16 NACA 0015 C_T values at 5kPa, all speeds, and all AOA.

2.7. Difficulties

The blades could not be printed horizontally because of two main reasons. First, when printed horizontally, the necessary support material would become stuck to the surface making it very rough and uneven. At that point the time needed to sand off these imperfections would have been too great and the result would not have been as clean. Secondly the blade would sometimes detach from the bed while being made, creating an arc that warped the design of the profile itself. In addition for the DF102, E10 and E178 profiles only experiments at 4 and 5 kPa and speeds of 2250 and 2500 could be carried out. This was due to the increase of vibrations that damaged the LMD base at the end of the experiments and the lack of a sensitive enough strain sensor at the beginning of the experiments. Future research should seek to resolve these issues so as to further improve on the experimental design.

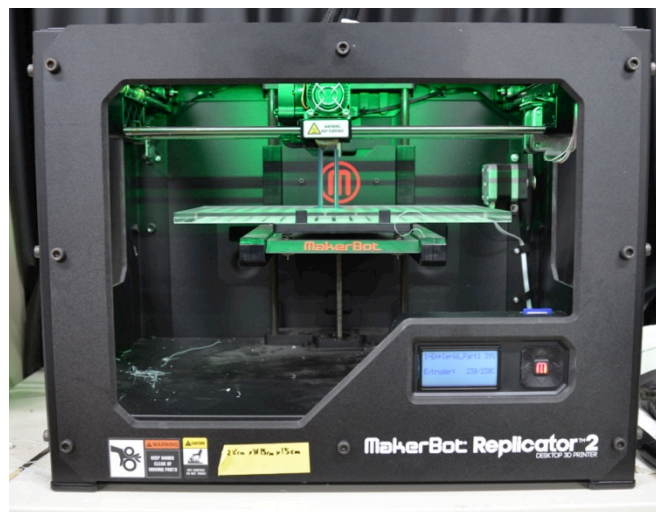


Figure 18 *MakerBot Replicator 2 printing two airfoils.*

3. Post Processing

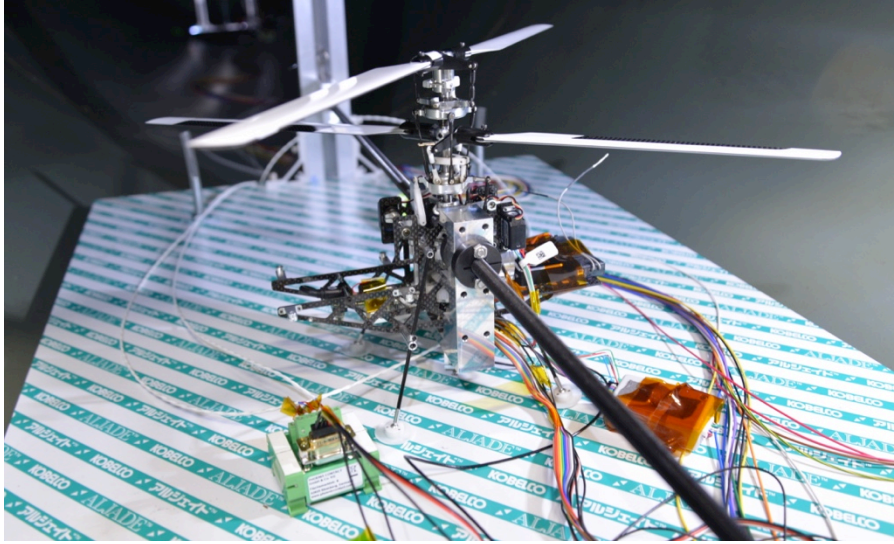


Figure 19 Close up of the helicopter fixed to the LMD.

As previously explained, in order to be able to compare the various C_T , all the results are shown at the same Reynolds number, meaning that for the nominal blade, which has a chord of only 2 cm (half of that of the other profiles which have a 4 cm chord), the speeds and pressures were quite different. It is also important to note that if for the nominal blade the radius length was 0.234 m, for all of the other blades that number dropped to 0.17 m. For example, in order to achieve $Re = 2400$, the triangular airfoil was spinning in a 3 kPa environment at a speed of 2250 rpm, while the nominal airfoil was spinning in a 4 kPa environment at a speed of 2500 rpm. Although Mach number should also be taken into consideration when comparing results, during these experiments this number was practically constant: minimum Mach number was 0.10 and maximum was 0.18. As may be seen from the graphed results in figure 20 to 25, the triangular airfoil is the best performing airfoil of all, as its values of C_T are always greater than the other profiles. Right after the triangular, the E178 profile, which has the smallest thickness of all, is also performing quite well. The difference in C_T between the nominal airfoil and the others is always more than double, meaning that chord length plays a very important role in thrust production. It is worth noting that although C_T for the nominal airfoil was always much lower than the others, due to its longer radius, the thrust produced was consistently much greater with respect to the shorter blades.

Values of C_T shown in tables 1 through 16 are now graphed in the following figures providing visual means to grasp the behavior of the airfoils.

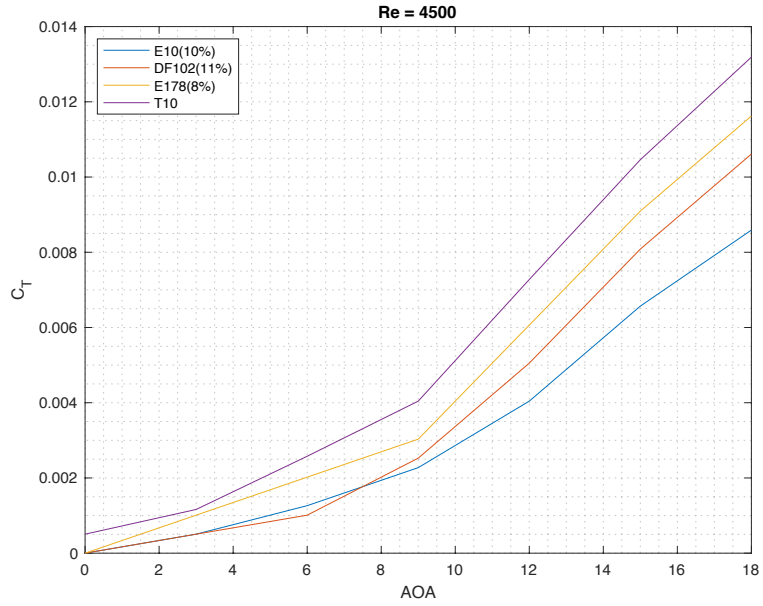


Figure 20 C_T comparison between various airfoils at $Re\ 4500$.

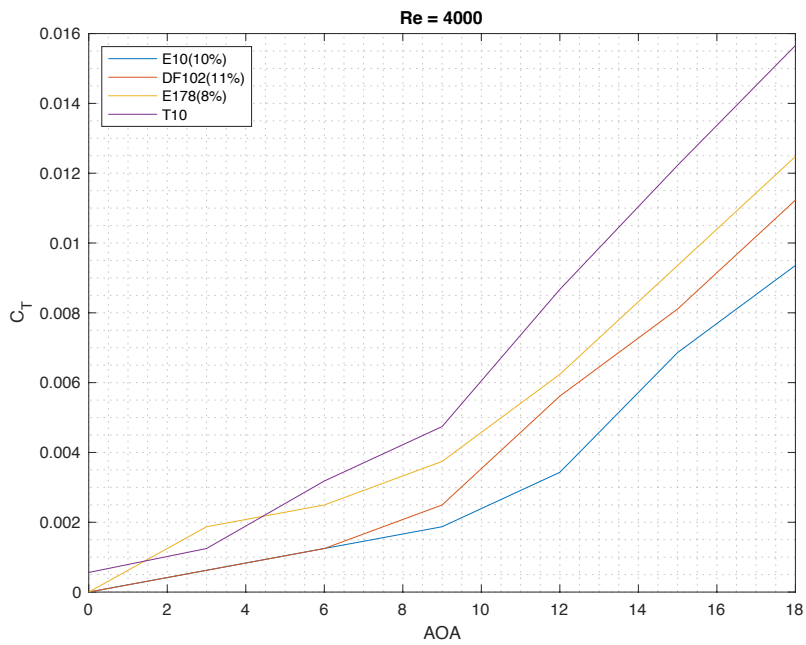


Figure 21 C_T comparison between various airfoils at $Re\ 4000$.

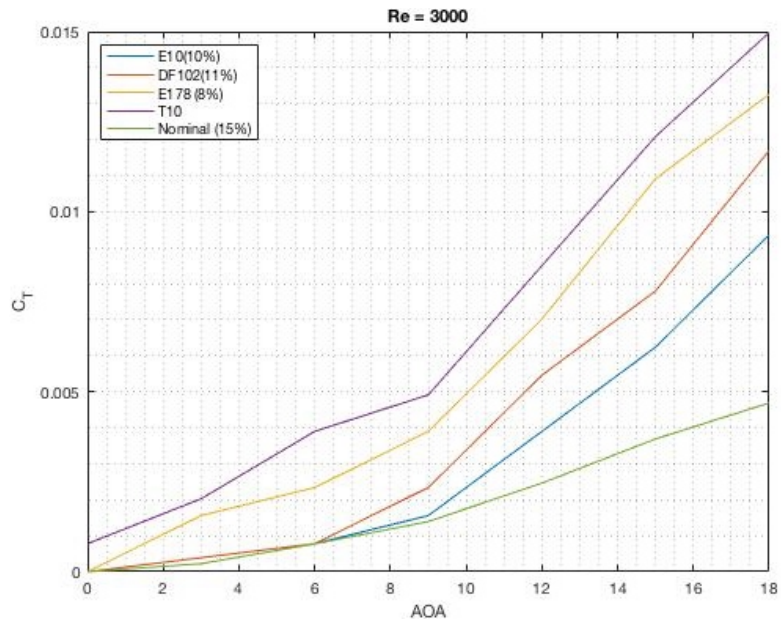


Figure 22 C_T comparison between all airfoils at Re 3000.

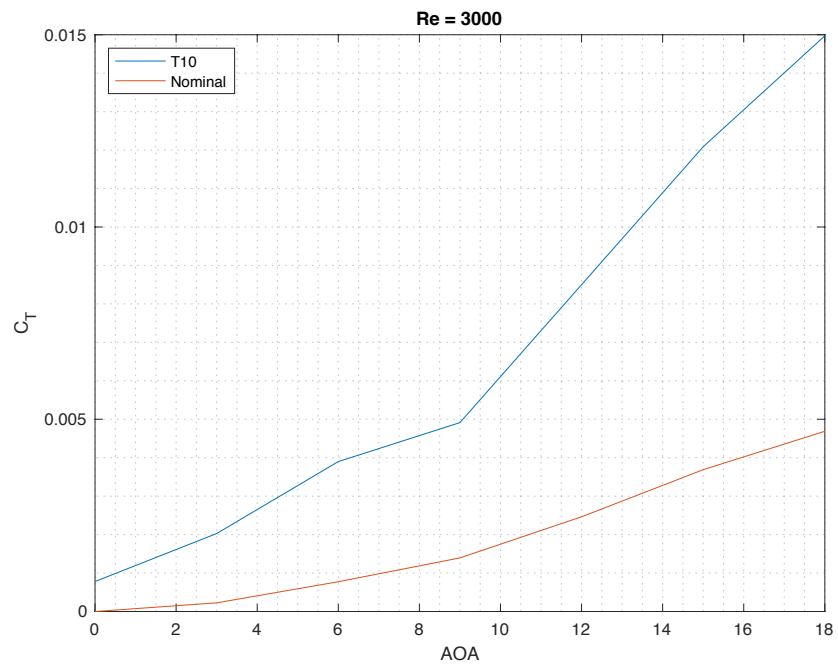


Figure 23 C_T comparisons between Triangular (T10) and NACA 0015 (nominal) airfoils at Re 3000.

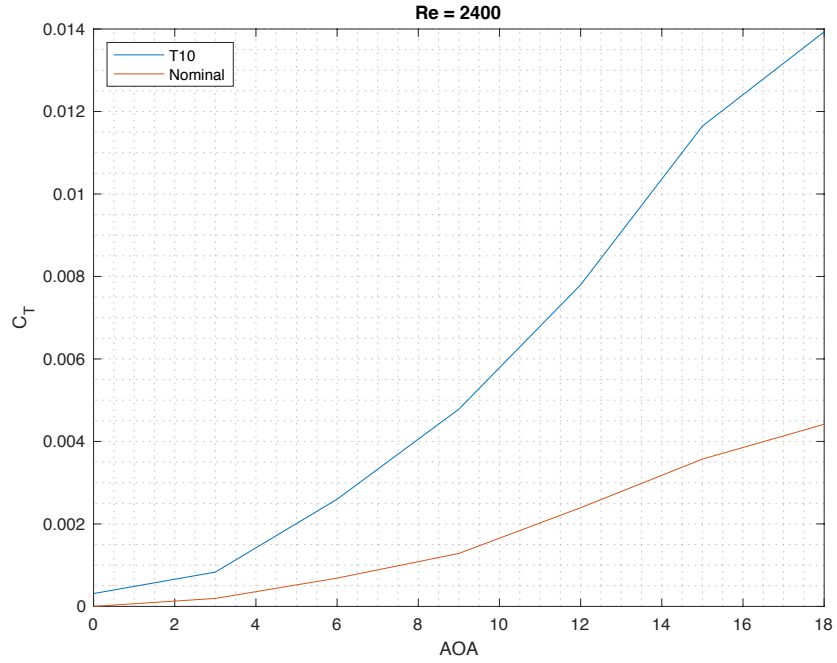


Figure 24 C_T comparison between Triangular (T10) and NACA 0015 (nominal) airfoils at Re 2400.

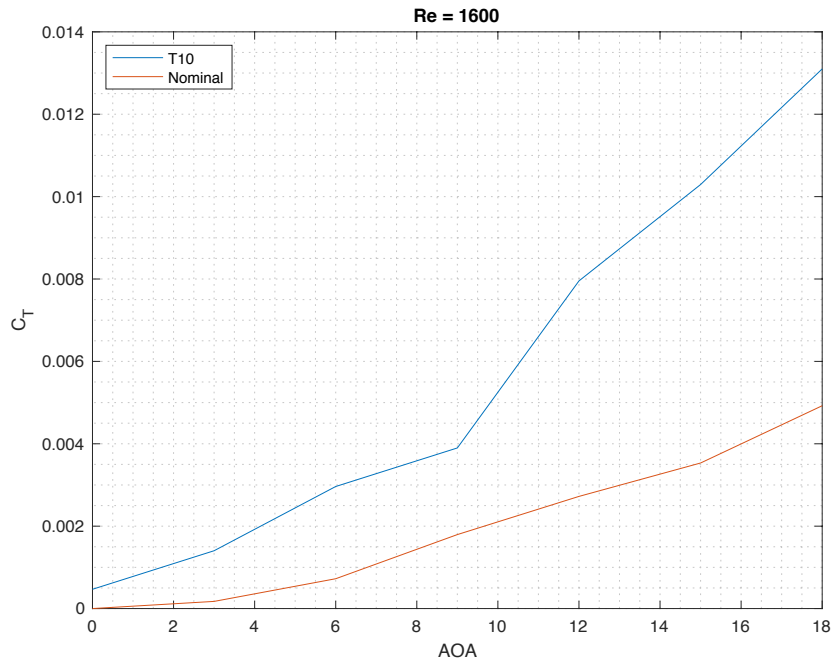


Figure 25 C_T comparison between Triangular (T10) and NACA 0015 (nominal) airfoils at Re 1600.

By looking at figures 26 and 27, it is noticeable how the nominal blade has indeed a low C_T but it is rather constant with changing Reynolds number: the total displacement is about 0.001, which corresponds to a 25% decrease. On the other hand, the triangular airfoil is behaving quite well until Reynolds 800 where it has a huge drop in performance: total displacement is now 0.006 which corresponds to a 40% decrease. That Reynolds number condition corresponded to a speed of 2000 rpm at a pressure of 1 kPa, which is not likely to happen as that rotation speed is rather small. Therefore, if we ignore that last condition, the maximum drop for the triangular airfoil becomes 0.002 or a 13% decrease. On top of this, the triangular airfoil has another advantage on the nominal blade: thrust production is essentially linear at low Reynolds numbers as can be observed comparing the curves at Re 800 for the triangular and Re 500 for the nominal blade. This linearity keeps the required control rule fairly simple, easing the calculations for optimization purposes.

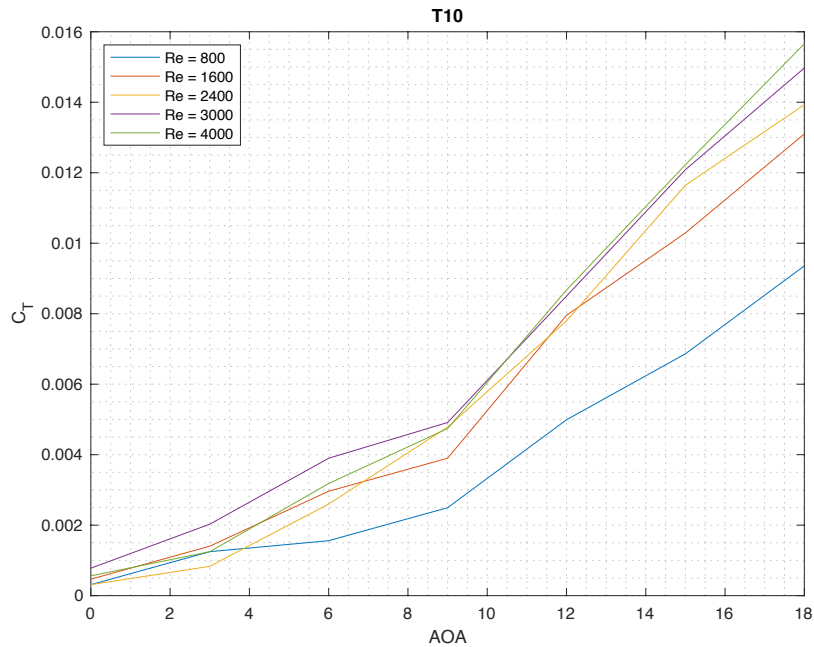


Figure 26 C_T comparison at various Reynolds for Triangular airfoil.

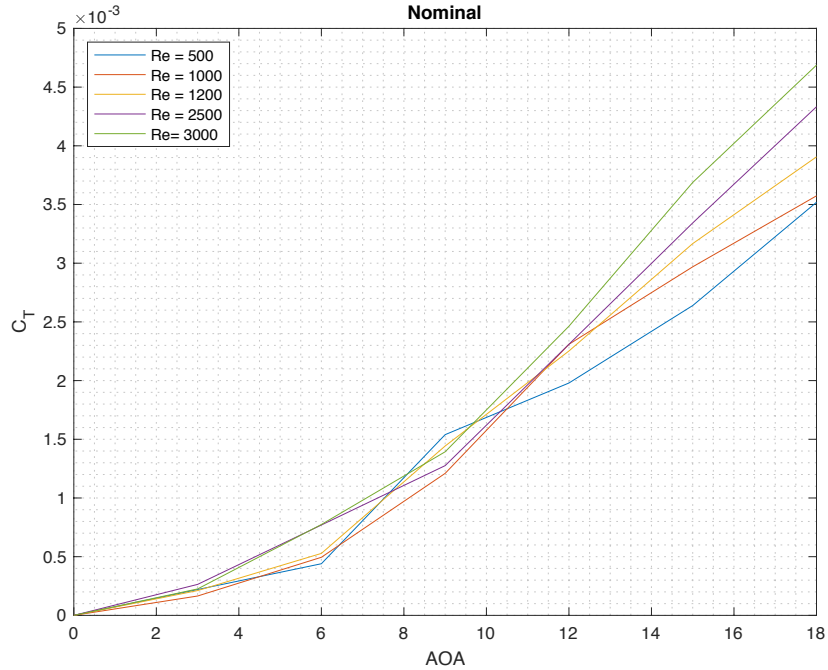


Figure 27 C_T comparison at various Reynolds for NACA 0015 airfoil.

Another peculiar feature of the triangular airfoil becomes evident after further observation of figure 26. It can be noticed how the slopes of every curve have a sharp increase once the angle of attack reaches a value around 9° . This rise in slope converts into higher thrust production. It has been confirmed by CFD analysis (reference [24,25,26]) that this is due to a separation bubble that is created between the leading edge and the point of maximum thickness or between the latter and the trailing edge. As portrayed in figure 28, after such an angle, the airflow detaches as soon as it reaches the body and then reattaches generating the separation bubble. On the other hand, in figure 29 the second possibility is reported according to CFD calculation carried out in reference [25]. These bubbles are characterized by a rather large pressure drop, which in turn, coupled with the almost unchanged pressure under the airfoil creates a considerable amount of thrust.

It becomes clear that even though the triangular airfoil presents sharp edges, the fluid around it manages to create a cushion like flow that gives a different shape to the airfoil as shown by the streamlines in figure 29. This cushion tends to take the shape of a more efficient airfoil thus increasing C_T production. At first glance, it would seem that with lower Reynolds number this behavior becomes weaker and weaker, with a big setback when the Reynolds number drops to 800, which is reasonable since the design Reynolds number is 3000 for this airfoil.

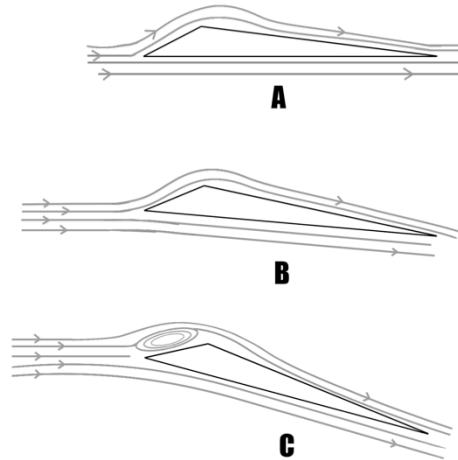


Figure 28 Triangular airfoil separation bubble formation while horizontal (A) $AOA < 9^\circ$ (B) and $AOA > 9^\circ$ (C)

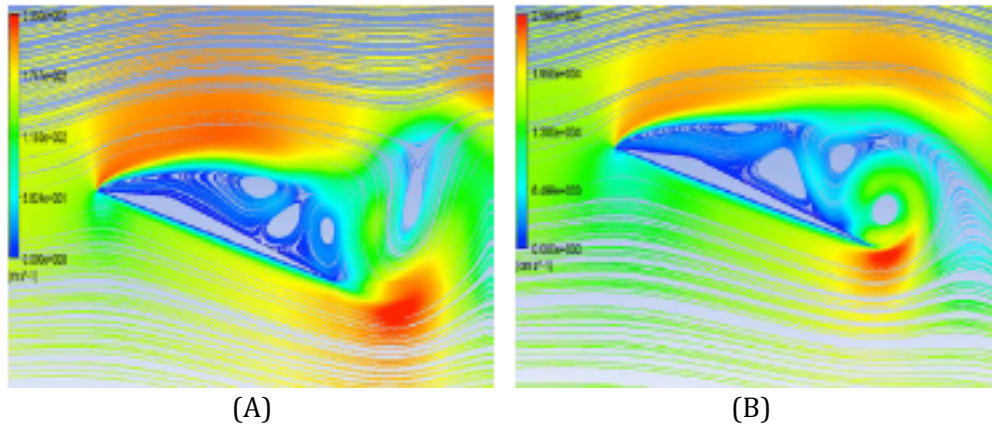


Figure 29 Triangular airfoil CFD for 12° (A) and 14° (B) according to Yang's research [25]

However, a counter-intuitive response is observed for the E178 airfoil, shown in figure 30. The behavior of this profile actually improves as Reynolds number decreases. This increase is close to the triangular reduction as the E178's coefficient of thrust undergoes a maximum growth of 0.0016 or 11%. These findings should be confirmed with further experimenting considering that the Reynolds number was not as low as the triangular or nominal airfoils.

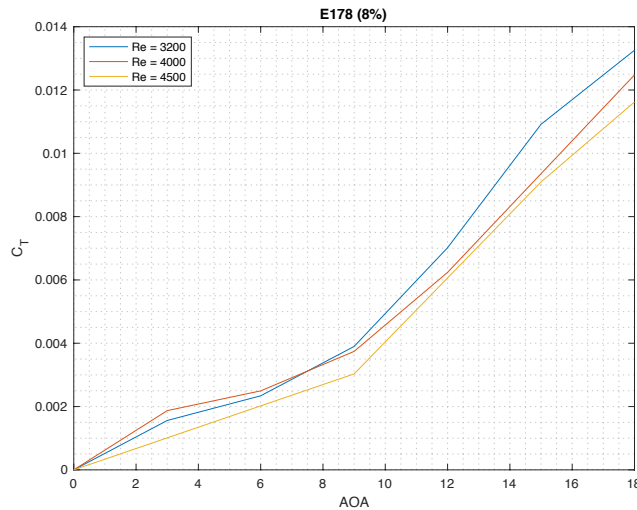


Figure 30 C_T comparison at various Reynolds for E178 airfoil.

In addition, after observing figure 31 and 32, it becomes clear how a bigger camber provides larger thrust production. E10 and DF102 profile were chosen as samples because their thickness is almost identical (10% and 11% respectively). Comparing the two at the same Reynolds number clearly shows the effect of their different camber: DF102's camber is 2.4% positioned at 43.5% of the chord while E10's camber is as low as 0.3% positioned at 31.9% of the chord. At a Reynolds number of 3200 and an angle of attack of 12°, the maximum difference in C_T production due to camber is 40%: E10's C_T is 0.003899 while DF102's is 0.005458. When increasing Reynolds number to 4000, C_T enhancement jumps to 63%: in this case the C_T for E10 is 0.003431 while for DF102 this value raises to 0.005614, while angle of attack remains 12°. These experiments draw the conclusion that camber positive effects weakens with lower Reynolds numbers.

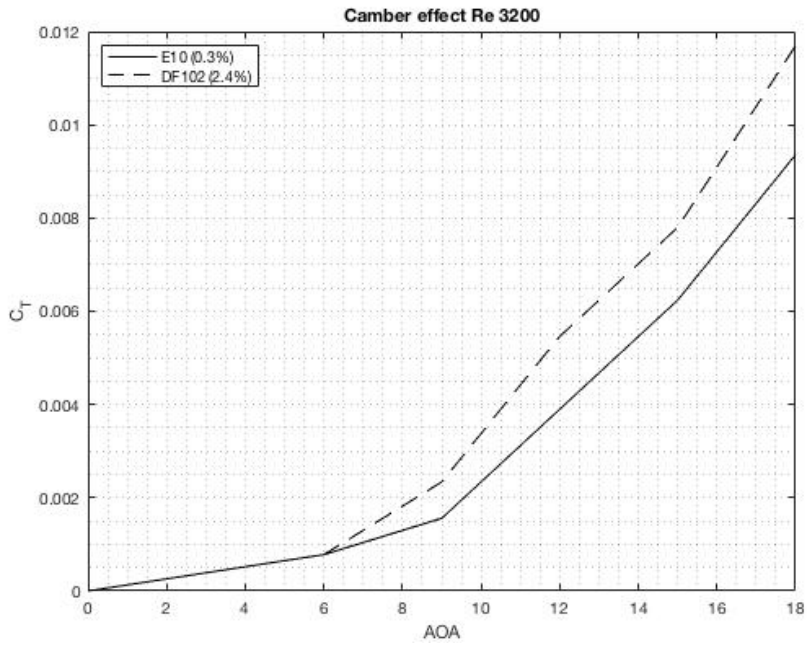


Figure 31 Effect of Camber on C_D at Re 3200.

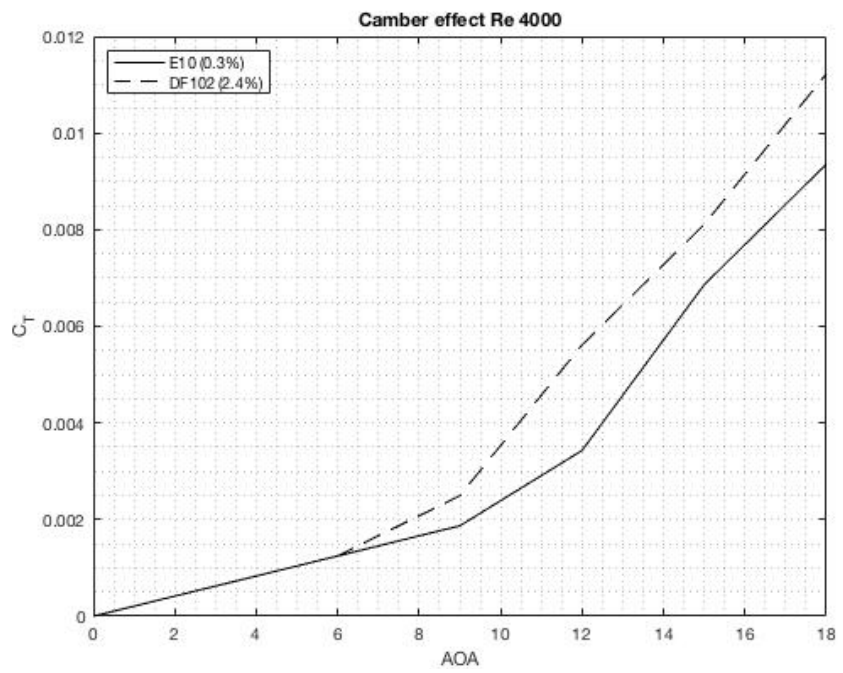
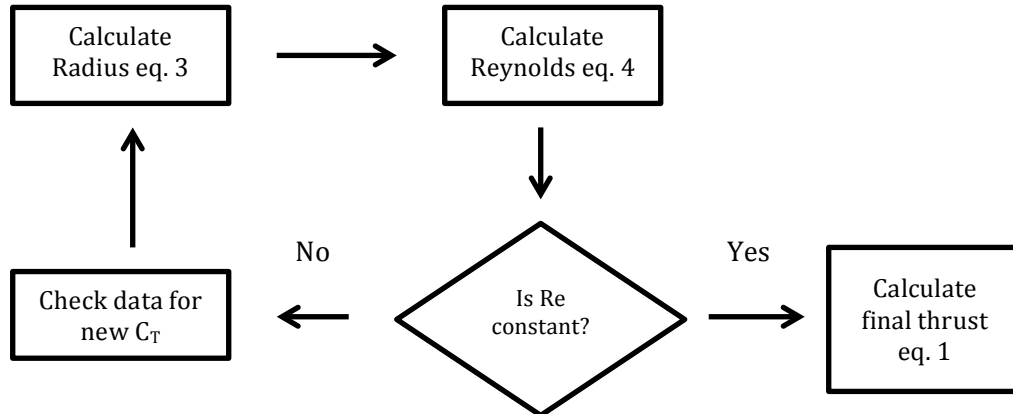


Figure 32 Effect of Camber on C_D for Re 4000

3.1. New rotor design

The main concern of this project is whether the helicopter would be able to fly or not in a Martian environment. At the current state, the rotor is too short to generate enough thrust to lift up the aircraft in a low-pressure environment; however, with all the information unveiled above it is possible to come up with the necessary rotor radius. To help visualize the steps taken to reach the optimal value the following flow-chart is shown and explained.



To calculate this new parameter, equation (3) was used with initial values of:

- $T = 300\text{g} = 3\text{N}$
- $\Omega = 2500\text{ rpm}$
- $\rho = 1\text{ kPa}$
- $C_T = 0.009347$ (from table 7)

Except for C_T all of the above parameters will remain constant during every iteration. Using equation (4), the Reynolds number linked to this new radius is calculated. Knowing the Reynolds number, the actual C_T is found in the tables and substituted to the previous one. At this point the whole calculation is carried out again and again until the Reynolds number remains basically constant. Eventually this leads to a radius length of 0.462 m correlated with $Re = 2400$ a C_T of 0.01393, Mach = 0.35 and an actual thrust generated of 3.3 N. When translated on Mars' conditions (previously cited gas constants and temperature of 5 °C), these values change to $Re = 3000$, $C_T = 0.01497$, Mach = 0.47 and generated thrust 3.4 N. Therefore confirming that, as hypothesized initially, a radius of 0.5 m is enough to allow the helicopter to hover in the harsh Mars environment. It is important to point out that blade extension comes with a weight increase that should partially be removed using the counter weights.

4. Conclusions

This research has experimentally confirmed several aerodynamic properties of a development Mars helicopter and determined new airfoils characteristics that are worthy of a further investigation. For starters, thrust is directly proportional to the fourth power of radius. As an example, at $Re = 2400$ and an angle of attack of 18° even if the triangular airfoil (0.17m radius) had a C_T of 0.01393 and the nominal airfoil (0.234m radius) had only 0.00442 the actual thrust produced was respectively 13.4g and 25.1g. Another demonstrated property is how thinner airfoils show to have better performance when Reynolds number diminishes. This is indicated by higher C_T values of the triangular and E178 airfoils (10% and 8% thickness) with respect to all of the other profiles (which range from 11% to 15% thickness). Same behavior is observed for increasing camber shown by the better performance of the DF102 airfoil (thickness 11%, camber 2.4%) over the E10 (thickness 10%, camber 0.3%). Also, due to the possible formation on the triangular airfoil of a reattached separation bubble, which rounds off the profile sharp edges, better performance is achieved by this particular profile with respect to the other airfoils. Reynolds number reduction is shown to be detrimental for all airfoils except for the E178 though this should be confirmed through further experiments in future studies. Another point that needs to be checked is how chord length affects thrust production. It can be deduced from this data that longer chords mean higher thrust although the extent of this phenomenon is not yet clear.

4.1. Possible Future Work

Several possibilities for future investigations arise as a result of this research project. Additional trials and measurements should be performed to perfectly grasp the behavior of airfoils at such low Reynolds number. Some additional experiments ideas that arose during this work are:

- Increase rotor radius to allow the helicopter to hover inside of the vacuum chamber. A strengthening of the swash plate will probably be necessary, as centrifugal force will be much higher.
- Effect of airfoil chord length on thrust and needed power, and understanding at what point this length actually becomes detrimental.
- A specific ultra low Reynolds number airfoil, shown in appendix, should be manufactured and tested to check if that design is compatible with the helicopter needs. It could be that C_T is high but material tensile or shear strengths are too low due to the very small thickness.
- Increase collector range to reach stall point and observe how Reynolds number affects it. Throughout this new experiment, maximum C_T will be reached and the airfoil's full potential will be exploited.
- Ground effect and rotor-on-rotor influence extent.
- Perform new experiments with the E178 airfoil to further verify the previous results.
- Perform torque measurements.

5. Appendix

5.1. Hovering Helicopter Thrust

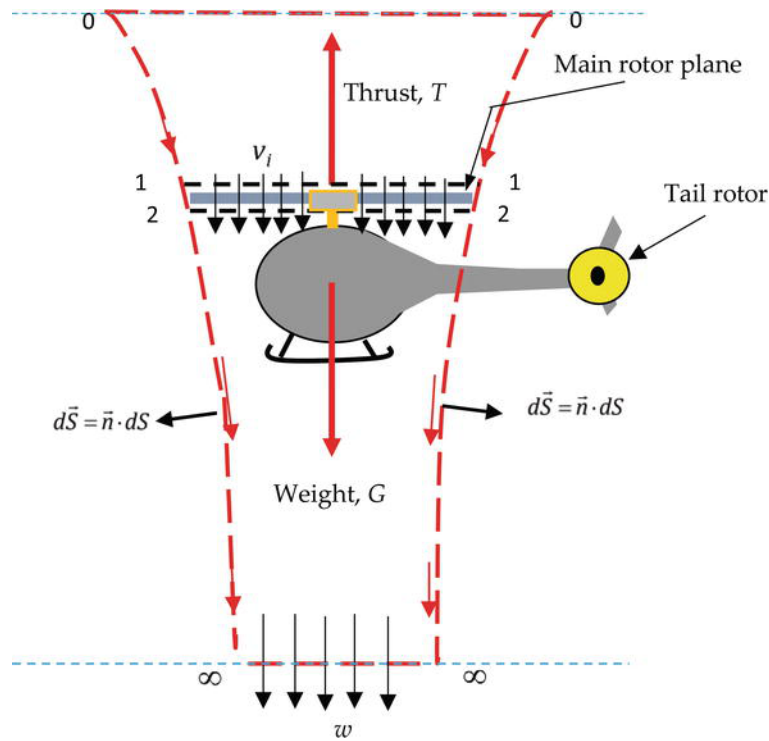


Figure 33 Helicopter in hovering flight []

Taking as reference figure 33 we can distinguish: section 0-0 which is the plane far upstream of the rotor (where air velocity is null); sections 1-1, and 2-2 that are the planes just above and below the rotor disk, and the far wake section ∞ . Between section 1-1 and 2-2- the flux moves at the induced velocity v_i and in the far wake the flux velocity is w . According to the Reynolds Transport Theorem, for a control volume surrounding the rotor and its wake (red dashed lines in figure 33) and defining $d\vec{S} = \vec{n} \cdot dS$, where the unit normal area vector \vec{n} is oriented outward, for any extensive parameter K , where $K = k \cdot \text{mass (m)}$, the following equation is valid:

$$\left(\frac{dK}{dt}\right)_{system} = \frac{\partial}{\partial t} \iiint \rho k dV + \iint \rho k \vec{V} \cdot d\vec{S} \quad (A1)$$

Where,

\vec{V} = local flow velocity.

m = mass of the fluid.

ρ = density of the fluid.

If we consider a steady flow the previous equation simplifies to:

$$\left(\frac{dK}{dt}\right)_{system} = \iint \rho k \vec{V} \cdot d\vec{S} \quad (A2)$$

Substituting to k, in equation A2, the values 1, \vec{V} , and $\frac{1}{2}V^2$ we obtain respectively the conservation of mass, momentum and energy.

Conservation of mass (k = 1)

$$\left(\frac{dm}{dt}\right)_{system} = \iint \rho \vec{V} \cdot d\vec{S} \quad (A3)$$

From this equation we can derive the mass flow rate, which is set at 0 since we considered a steady-flow.

$$0 = \iint_{2-2} -\rho v_i dS + \iint_{\infty} \rho w dS \quad (A4)$$

Consequently,

$$\rho v_i A = \rho w A_{\infty} \quad (A5)$$

Conservation of momentum (k = \vec{V})

$$\left(\frac{d(m\vec{V})}{dt}\right)_{system} = \iint \rho \vec{V} \vec{V} \cdot d\vec{S} \quad (A6)$$

The left end side of equation A6 is the summation of all of the forces applied on the control volume, in this case thrust (T) while the right hand side introduces the mass flow rate \dot{m} and develops as follows:

$$T = w \iint_{\infty} \rho w dS = w \dot{m} \quad (A7)$$

Conservation of energy (k = $\frac{1}{2}V^2$)

$$\left(\frac{dE}{dt}\right)_{system} = \iint \rho \frac{1}{2} V^2 \vec{V} \cdot d\vec{S} \quad (A8)$$

$\frac{dE}{dt}$ is the power absorbed by the rotor and it is equal to Tv_i , thus,

$$T v_i = \iint \rho \frac{1}{2} V^2 \vec{V} \cdot d\vec{S} = \frac{1}{2} w^2 \dot{m} \quad (A9)$$

Where the right end side is none other than the work done on the rotor. Substituting equation A7 into A10 we derive:

$$\dot{m} w v_i = \frac{1}{2} w^2 \dot{m} \quad \rightarrow \quad v_i = \frac{1}{2} w \quad (A10)$$

Finally combining equation A1 and A7 we get:

$$T = \dot{m}w = \dot{m}2v_i = \rho Av_i 2v_i = 2\rho Av_i^2 \quad (A11)$$

The induced velocity is then normalized using rotor's radius and angular velocity ($R\Omega$) also introducing C_T as T normalized by dynamic pressure obtaining:

$$C_T = \frac{T}{\rho A \Omega^2 R^2} \quad (A12)$$

Note that since in the experiment there are two rotor disks, thrust measured was halved in order to work with single rotor readings.

5.2. Experimental Airfoil for ultra low Reynolds number

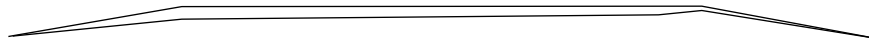


Figure 34 Experimental Ultra low Reynolds number airfoil

This airfoil is especially made for ultra low Reynolds number but couldn't be produced in time. Therefore it would be interesting to see how it behaves and if its mechanical characteristics are good enough for the helicopter's needs. Coordinates for this experimental airfoil are shown below. If the produced C_T is much higher then the other airfoil, this profile could drastically reduce rotor length, thus weight of the single blade. Due to the lower blade weight a higher rotor speed can be reached without reaching critical centrifugal forces.

X	Y	X	Y	X	Y
1.000000	-0.002000	0.805000	0.034075	0.610000	0.034842
0.995000	-0.001075	0.800000	0.035000	0.605000	0.034838
0.990000	-0.000150	0.795000	0.034996	0.600000	0.034833
0.985000	0.000775	0.790000	0.034992	0.595000	0.034829
0.980000	0.001700	0.785000	0.034988	0.590000	0.034825
0.975000	0.002625	0.780000	0.034983	0.585000	0.034821
0.970000	0.003550	0.775000	0.034979	0.580000	0.034817
0.965000	0.004475	0.770000	0.034975	0.575000	0.034813
0.960000	0.005400	0.765000	0.034971	0.570000	0.034808
0.955000	0.006325	0.760000	0.034967	0.565000	0.034804
0.950000	0.007250	0.755000	0.034963	0.560000	0.034800
0.945000	0.008175	0.750000	0.034958	0.555000	0.034796
0.940000	0.009100	0.745000	0.034954	0.550000	0.034792
0.935000	0.010025	0.740000	0.034950	0.545000	0.034788
0.930000	0.010950	0.735000	0.034946	0.540000	0.034783
0.925000	0.011875	0.730000	0.034942	0.535000	0.034779
0.920000	0.012800	0.725000	0.034938	0.530000	0.034775
0.915000	0.013725	0.720000	0.034933	0.525000	0.034771
0.910000	0.014650	0.715000	0.034929	0.520000	0.034767
0.905000	0.015575	0.710000	0.034925	0.515000	0.034763
0.900000	0.016500	0.705000	0.034921	0.510000	0.034758
0.895000	0.017425	0.700000	0.034917	0.505000	0.034754
0.890000	0.018350	0.695000	0.034913	0.500000	0.034750
0.885000	0.019275	0.690000	0.034908	0.495000	0.034746
0.880000	0.020200	0.685000	0.034904	0.490000	0.034742
0.875000	0.021125	0.680000	0.034900	0.485000	0.034738
0.870000	0.022050	0.675000	0.034896	0.480000	0.034733
0.865000	0.022975	0.670000	0.034892	0.475000	0.034729
0.860000	0.023900	0.665000	0.034888	0.470000	0.034725
0.855000	0.024825	0.660000	0.034883	0.465000	0.034721
0.850000	0.025750	0.655000	0.034879	0.460000	0.034717
0.845000	0.026675	0.650000	0.034875	0.455000	0.034713
0.840000	0.027600	0.645000	0.034871	0.450000	0.034708
0.835000	0.028525	0.640000	0.034867	0.445000	0.034704
0.830000	0.029450	0.635000	0.034863	0.440000	0.034700
0.825000	0.030375	0.630000	0.034858	0.435000	0.034696
0.820000	0.031300	0.625000	0.034854	0.430000	0.034692
0.815000	0.032225	0.620000	0.034850	0.425000	0.034688
0.810000	0.033150	0.615000	0.034846	0.420000	0.034684

X	Y
0.415000	0.034679
0.410000	0.034675
0.405000	0.034671
0.400000	0.034667
0.395000	0.034663
0.390000	0.034658
0.385000	0.034654
0.380000	0.034650
0.375000	0.034646
0.370000	0.034642
0.365000	0.034638
0.360000	0.034633
0.355000	0.034629
0.350000	0.034625
0.345000	0.034621
0.340000	0.034617
0.335000	0.034613
0.330000	0.034608
0.325000	0.034604
0.320000	0.034600
0.315000	0.034596
0.310000	0.034592
0.305000	0.034588
0.300000	0.034583
0.295000	0.034579
0.290000	0.034575
0.285000	0.034571
0.280000	0.034567
0.275000	0.034563
0.270000	0.034558
0.265000	0.034554
0.260000	0.034550
0.255000	0.034546
0.250000	0.034542
0.245000	0.034538
0.240000	0.034533
0.235000	0.034529
0.230000	0.034525
0.225000	0.034521
0.220000	0.034517
0.215000	0.034513
0.210000	0.034508
0.205000	0.034504
0.200000	0.034500
0.195000	0.033638
0.190000	0.032775
0.185000	0.031913
0.180000	0.031050
0.175000	0.030188
0.170000	0.029325
0.165000	0.028463
0.160000	0.027600
0.155000	0.026738
0.150000	0.025875
0.145000	0.025013
0.140000	0.024150
0.135000	0.023288
0.130000	0.022425
0.125000	0.021562
0.120000	0.020700
0.115000	0.019838
0.110000	0.018975
0.105000	0.018113
0.100000	0.017250
0.095000	0.016387
0.090000	0.015525
0.085000	0.014663
0.080000	0.013800
0.075000	0.012938
0.070000	0.012075
0.065000	0.011213
0.060000	0.010350
0.055000	0.009487
0.050000	0.008625
0.045000	0.007762
0.040000	0.006900
0.035000	0.006037
0.030000	0.005175
0.025000	0.004312
0.020000	0.003450
0.015000	0.002587
0.010000	0.001725
0.005000	0.000863
0.000000	0.000000
0.005000	0.000500
0.010000	0.001000
0.015000	0.001500
0.020000	0.002000
0.025000	0.002500
0.030000	0.003000
0.035000	0.003500

X	Y
0.040000	0.004000
0.045000	0.004500
0.050000	0.005000
0.055000	0.005500
0.060000	0.006000
0.065000	0.006500
0.070000	0.007000
0.075000	0.007500
0.080000	0.008000
0.085000	0.008500
0.090000	0.009000
0.095000	0.009500
0.100000	0.010000
0.105000	0.010500
0.110000	0.011000
0.115000	0.011500
0.120000	0.012000
0.125000	0.012500
0.130000	0.013000
0.135000	0.013500
0.140000	0.014000
0.145000	0.014500
0.150000	0.015000
0.155000	0.015500
0.160000	0.016000
0.165000	0.016500
0.170000	0.017000
0.175000	0.017500
0.180000	0.018000
0.185000	0.018500
0.190000	0.019000
0.195000	0.019500
0.200000	0.020000
0.205000	0.020045
0.210000	0.020091
0.215000	0.020136
0.220000	0.020182
0.225000	0.020227
0.230000	0.020273
0.235000	0.020318
0.240000	0.020364
0.245000	0.020409
0.250000	0.020455
0.255000	0.020500
0.260000	0.020545
0.265000	0.020591
0.270000	0.020636
0.275000	0.020682
0.280000	0.020727
0.285000	0.020773
0.290000	0.020818
0.295000	0.020864
0.300000	0.020909
0.305000	0.020955
0.310000	0.021000
0.315000	0.021045
0.320000	0.021091
0.325000	0.021136
0.330000	0.021182
0.335000	0.021227
0.340000	0.021273
0.345000	0.021318
0.350000	0.021364
0.355000	0.021409
0.360000	0.021455
0.365000	0.021500
0.370000	0.021545
0.375000	0.021591
0.380000	0.021636
0.385000	0.021682
0.390000	0.021727
0.395000	0.021773
0.400000	0.021818
0.405000	0.021864
0.410000	0.021909
0.415000	0.021955
0.420000	0.022000
0.425000	0.022045
0.430000	0.022091
0.435000	0.022136
0.440000	0.022182
0.445000	0.022227
0.450000	0.022273
0.455000	0.022318
0.460000	0.022364
0.465000	0.022409
0.470000	0.022455
0.475000	0.022500
0.480000	0.022545
0.485000	0.022591
0.490000	0.022636

X	Y
0.495000	0.022682
0.500000	0.022727
0.505000	0.022773
0.510000	0.022818
0.515000	0.022864
0.520000	0.022909
0.525000	0.022955
0.530000	0.023000
0.535000	0.023045
0.540000	0.023091
0.545000	0.023136
0.550000	0.023182
0.555000	0.023227
0.560000	0.023273
0.565000	0.023318
0.570000	0.023364
0.575000	0.023409
0.580000	0.023455
0.585000	0.023500
0.590000	0.023545
0.595000	0.023591
0.600000	0.023636
0.605000	0.023682
0.610000	0.023727
0.615000	0.023773
0.620000	0.023818
0.625000	0.023864
0.630000	0.023909
0.635000	0.023955
0.640000	0.024000
0.645000	0.024045
0.650000	0.024091
0.655000	0.024136
0.660000	0.024182
0.665000	0.024227
0.670000	0.024273
0.675000	0.024318
0.680000	0.024364
0.685000	0.024409
0.690000	0.024455
0.695000	0.024500
0.700000	0.024545
0.705000	0.024591
0.710000	0.024636
0.715000	0.024682
0.720000	0.024727
0.725000	0.024773
0.730000	0.024818
0.735000	0.024864
0.740000	0.024909
0.745000	0.024955
0.750000	0.025000
0.755000	0.025500
0.760000	0.026000
0.765000	0.026500
0.770000	0.027000
0.775000	0.027500
0.780000	0.028000
0.785000	0.028500
0.790000	0.029000
0.795000	0.029500
0.800000	0.030000
0.805000	0.029200
0.810000	0.028400
0.815000	0.027600
0.820000	0.026800
0.825000	0.026000
0.830000	0.025200
0.835000	0.024400
0.840000	0.023600
0.845000	0.022800
0.850000	0.022000
0.855000	0.021200
0.860000	0.020400
0.865000	0.019600
0.870000	0.018800
0.875000	0.018000
0.880000	0.017200
0.885000	0.016400
0.890000	0.015600
0.895000	0.014800
0.900000	0.014000
0.905000	0.013200
0.910000	0.012400
0.915000	0.011600
0.920000	0.010800
0.925000	0.010000
0.930000	0.009200
0.935000	0.008400
0.940000	0.007600
0.945000	0.006800

X	Y
0.950000	0.006000
0.955000	0.005200
0.960000	0.004400
0.965000	0.003600

X	Y
0.970000	0.002800
0.975000	0.002000
0.985000	0.000400
0.980000	0.001200

X	Y
0.990000	-0.000400
0.995000	-0.001200

5.3. Weight reduction

When Martian gravity is considered the helicopter will surely weight less then on Earth. If feasibility is concerned this is an important parameter that can determine whether a mission is doable or not. The weight reduction was calculated considering the difference in weight between the helicopter on Earth and on Mars added to the structure weight as so:

$$W_{reduct} = m_{heli} \cdot g_{Earth} - m_{heli} \cdot g_{Mars} + W_{struct} = m_{heli}(g_{Earth} - g_{Mars}) + W_{struct}$$

It was then transformed into the required Earth's mass and divided in two counterweights as explained in section 2.2.

Bibliography

- [1] "A Preliminary Systems Engineering Study on a Concept for Mars Exploration with an Unmanned Autonomous Vehicle and Ground Rover Configuration". Michel Lacerda, Dongjin Park, Srujal Patel, Daniel Schrage. Georgia Institute of Technology. (2018)
- [2] "A Study on a Miniature Rotary-Wing Vehicle for Mars Exploration: Its Feasibility and Aerodynamic Characteristics of the Rotor". Noriaki Tsuzuki. University of Tokyo. (2005)
- [3] "Aerodynamics and Design for Ultra-Low Reynolds Number Flight". Peter J. Kunz. Stanford University. (2003)
- [4] "Aeromechanical Loads on a Mars Coaxial Rotor". Daniel Escobar, Inderjit Chopra, Anubhav Datta. Maryland College Park. (2018)
- [5] "Airplane Propeller Design in Low-Reynolds Number Flows". Naoki Yoshida, Genki Nakai, Koichi Yonezawa, Kento Abe, Shigeru Sunada, Kazuyasu Sugiyama. Osaka University. Osaka Prefecture University. (2015)
- [6] "An Experimental Study of Triangular Airfoils for Mars Airplane". Hidenori Hidaka, Masato Okamoto. Kanazawa Institute of Technology. (2013)
- [7] "Computational Aerodynamics Analysis of a Martian Rotorcraft". Kelly J. Corfeld, Roger C. Strawn, Lyle N. Long. Pennsylvania State University University Park. NASA Ames Research Center. (2004).
- [8] "Computational Analysis Of A Prototype Martian Rotorcraft Experiment." Kelly J. Corfeld, Roger C. Strawn, Lyle N. Long. Pennsylvania State University University Park. NASA Ames Research Center. (2002).
- [9] "Conceptual Helicopter Design for Exploration of Pit Craters and Caves on Mars" Risako Aoki, Akira Oyama Institute of Space and Astronautical Science, JAXA. (2019)
- [10] "Design and Fabrication of the Mars Helicopter Rotor, Airframe, and Landing Gear Systems" Benjamin T. Pipenberg, Matthew T. Keennon. Aerovironment, Inc. Jet Propulsion Laboratory (2019)
- [11] Electric motor specifications. https://www.jaxa.jp/press/2019/02/20190207a_j.html.
- [12] "Experimental Investigation and Demonstration of Rotary-Wing Technologies for Flight in the Atmosphere of Mars" L.A. Young, E.W. Aiken. (2002)
- [13] "Experimental Results for the Eppler 387 Airfoil at Low Reynolds Numbers in the Langley Low-Turbulence Pressure Tunnel" Robert J. McGhee, Betty S. Walker, and Betty F. Millard. Langley Research Center (1988)
- [14] "Experimental Study on High Efficiency of Aerodynamic Performance of Rotor Blades for Mars Helicopter" Kensuke Kanou, Koji Fujita. Tohoku University. Institute of Space and Astronautical Science, JAXA. (2019)
- [15] "Generation of Mars Helicopter Rotor Model for Comprehensive Analyses", Witold J. F. Koning, NASA Ames Research Center. (2018)
- [16] "Guidance and Control for a Mars Helicopter". Håvard Fjær Grip et al. JPL. NASA Ames Research Center. (2018)
- [17] "Helicopter Could Be 'Scout' for Mars Rovers,". JPL. 2015. [Online]. Available: <https://www.jpl.nasa.gov/news/news.php?feature=4457>. [Accessed: 12-Jun-2017].
- [18] "Low Reynolds Number Airfoil Evaluation for the Mars Helicopter Rotor". Witold J. F. Koning, Ethan A. Romander, Wayne Johnson. NASA Ames Research Center (2018)
- [19] "Mars Helicopter Technology Demonstrator" J. Bob Balaram et al. Jet Propulsion Laboratory, NASA Ames Research Center. (2018)

- [20] "Mars Rotorcraft: Possibilities, Limitations, and Implications For Human/Robotic Exploration". Larry A. Young, Geoffrey Briggs, Pascal Lee. NASA Ames Research Center. (2004)
- [21] "Measurements Comparing Hover Performance of Single, Coaxial, Tandem, and Tilt-Rotor Configurations" Manikandan Ramasamy. NASA Ames Research Center (2013)
- [22] "Reynolds number effects on aerodynamic performances of rotor in low Reynolds number conditions". Akira Oyama, Mitsuki Koh, Risako Aoki, Satoshi Sekimoto Institute of Space and Astronautical Science, JAXA.(2018)
- [23] "Airfoil coordinates and performance graphs" www.airfoiltools.com
- [24] "Numerical study on rotating flat airfoil under low Reynolds number condition using rFlow3D, Akira Oyama, Daichi Ogasawara. Institute of Space and Astronautical Science, JAXA.
- [25] "CFD Simulations of a Triangular Airfoil for Martian Atmosphere in Low-Reynolds Number Compressible Flow", Yang, Agarwal, Washington University. (2019)
- [26] "Nonlinear Lift on a Triangular Airfoil in Low-Reynolds-Number Compressible Flow", Mundai, Suwa, Florida State University, Tohoku University. (2015)
- [27] "Summary of Low speed Airfoil Data". Selig. DAAE, University of Illinois. (1995).
- [28] "Atypical pit craters on Mars: New insight from THEMIS, CTX, and HiRISE observations", Cushing, G.E., Okubo, C.H. and Titus, T.N. J. Geophys. Res. Planets, 120, 1023-1043, doi:10.1002/2014JE004735.
- [29] "Helicopter to accompany NASA's next Mars rover to Red Planet". Clark. (2018)
- [30] "Mars Helicopter Fact Sheet". NASA. (2020)